

Coherent control through phonon anharmonicity

Gili Scharf¹, Tomer Hasharoni¹, Lara Donval¹, Leah Ben Gur¹, Alon Ron¹

¹*Raymond and Beverly Sackler School of Physics and Astronomy, Tel-Aviv 69978, Israel*

Anharmonic lattice vibrations play a key role in many physical phenomena. They govern the heat conductivity of solids, strongly affect the phonon spectra, play a prominent role in soft mode phase transitions, allow ultrafast engineering of material properties and more. The most direct evidence for anharmonicity is to measure the oscillation frequency changing as a function of the oscillation amplitude. For lattice vibrations, this is not a trivial task, and anharmonicity is probed indirectly through its effects on thermodynamic properties and spectral features or through coherent decay of one mode to another. However, measurement of the anharmonicity of a single Raman mode is still lacking. We show that ultrafast double pump-probe spectroscopy could be used to directly observe frequency shifts of Raman phonons as a function of the oscillation amplitude and disentangle the coherent contributions from quasi-harmonic sources such as temperature and changes to the carrier density in the thermoelectric materials SnTe and SnSe. Our results have dramatic implications for the material engineering of future thermoelectrics. Moreover, our methodology could be used to isolate the basic mechanisms driving optically induced phase transitions and other nonlinear phenomena based on their unique timestamps.

The properties of phonons and their interplay with other constituents of a solid play a crucial role in determining material properties. One such property is the phonon anharmonicity, which

determines the lattice thermal conductivity, and understanding it is critical for the development and engineering of new thermoelectric and energy materials^{1,2}. Phonon anharmonicity could be indirectly probed by measuring the change in scattering or thermodynamic properties as a function of external stimuli such as temperature and pressure. For example, it can be observed as line-width broadening and changes to the phonon frequency, as well as variations in thermal conductivity or expansion^{3,4} as the temperature changes. Alternatively, its effects on the phonon spectrum could be probed through an inelastic scattering of neutrons¹ and X-rays⁵. Ultrafast pump-probe spectroscopy has also been used to observe anharmonic coupling between phonon modes. For example, Teitelbaum et al.⁶ showed that the A_{1g} phonon in excited bismuth decays to pairs of acoustic modes with opposite momenta which drove temporal oscillations at the corresponding frequency. Similarly, off-diagonal peaks in two-dimensional spectroscopy measure the coupling between different vibrational modes of molecules and solids⁷⁻¹⁰. Another example is the nonlinear coupling between infrared-active modes and symmetric Raman modes was observed by Först et al.¹¹, pioneering the field of nonlinear phononics. The common feature of all of these experiments is that they probed anharmonic coupling between different vibrational modes. However, to our knowledge, no experiment has yet measured the frequency shifts of a single mode resulting from variations in the oscillation amplitude.

Anharmonicity is particularly important in thermoelectric materials and controlling it, as well as the frequencies, lifetime, and dispersion of both acoustic and optical modes are utilized as control knobs for thermoelectric efficiency.¹² We chose to work with SnTe, a promising thermoelectric material¹³, whose anharmonicity is currently a topic of extensive study^{2,14-16}. Addi-

tionally, SnTe has recently gained further attention thanks to its topological crystalline insulator properties¹⁷. In this work, we directly measure the anharmonicity of a single phonon mode by utilizing double pump-probe spectroscopy, a technique used in the past to control phase transitions using light^{18–20}, to coherently control phonon oscillations^{6,21,22}, and more. Our findings reveal significant frequency shifts resulting from variations in oscillation amplitude. This method allows us to disentangle the contributions of different physical effects to ultrafast measurements using their temporal fingerprint such as thermal, electronic, and anharmonic effects on phonon behavior.

To excite coherent oscillations of the A_g mode, we utilize the "displacive excitation of coherent phonons" (DECP) process²³. Ultrashort laser pulses (70 and 126 fs) at 750 nm, resonant with a transition between Te and Sn bands, are incident on the sample, resulting in photo-excitation of electrons from the Te anion to the Sn cation. This reduces the charge difference between the ions, resulting in a softening of the chemical bond between them. The charge transfer shifts the equilibrium position of the ions closer to one another causing them to oscillate around the new equilibrium positions.

Figure 1(a) shows the relative change of sample reflectivity $\Delta R/R$ as a function of the time delay from a single pump excitation with an incident fluence of $0.68[mJ/cm^2]$ (which translates to excitation density of $\approx 4.46 \times 10^{21}[cm^{-3}]$ ²⁴). The signal could be decomposed to a decaying bi-exponential background overlaid with a damped oscillatory component. The colored solid lines in Figure 1(a) show the decomposition of the signal to its different components. We note that the oscillatory component displays a cosine-like behavior in agreement with the DECP mechanism²³.

The sign of the oscillatory component near time zero is positive. Understanding that the DECP mechanism in SnTe is initiated by bond softening enables us to use the positive sign of $\Delta R/R$ at time zero as a calibration, linking bond softening and the positive sign of the oscillatory component of $\Delta R/R$. The fast exponential component can be associated with electrons decaying back to their ground state due to the similar timescales observed using time-resolved photoemission²⁵. The slower exponential component can be associated with thermal relaxation effects between the electronic and phononic baths. Estimates of the expected time constants from known thermal conductivity and heat capacity of SnTe are shown in supplementary section 4. Figure 1(b) shows the fluence dependence of the $\Delta R/R$ signal of SnTe. The most striking aspect of the data is the redshift the oscillations exhibit towards higher fluences indicating strong softening of the mode as the fluence is increased. Dashed lines are used as a guide to the eye to mark the shift in the oscillation peaks as the fluence is varied. The shifts in peak positions are very small for the zero and first peaks and increase for the later peaks which is a signature that the shifts originate from changes in the oscillation frequency rather than its phase. Figure 1(c) shows the frequency that was extracted by fitting the data in Figure 1(b) as a function of the applied fluence. The magnitude of the phonon softening at the highest fluence is almost 20% lower than its value in equilibrium. An extrapolation of the oscillation frequency to zero fluence gives a frequency of 3.65 THz corresponding to 122 cm^{-1} , compatible with the known Ag phonon of SnTe²⁶ and our Raman measurements (inset), marked by a yellow star.

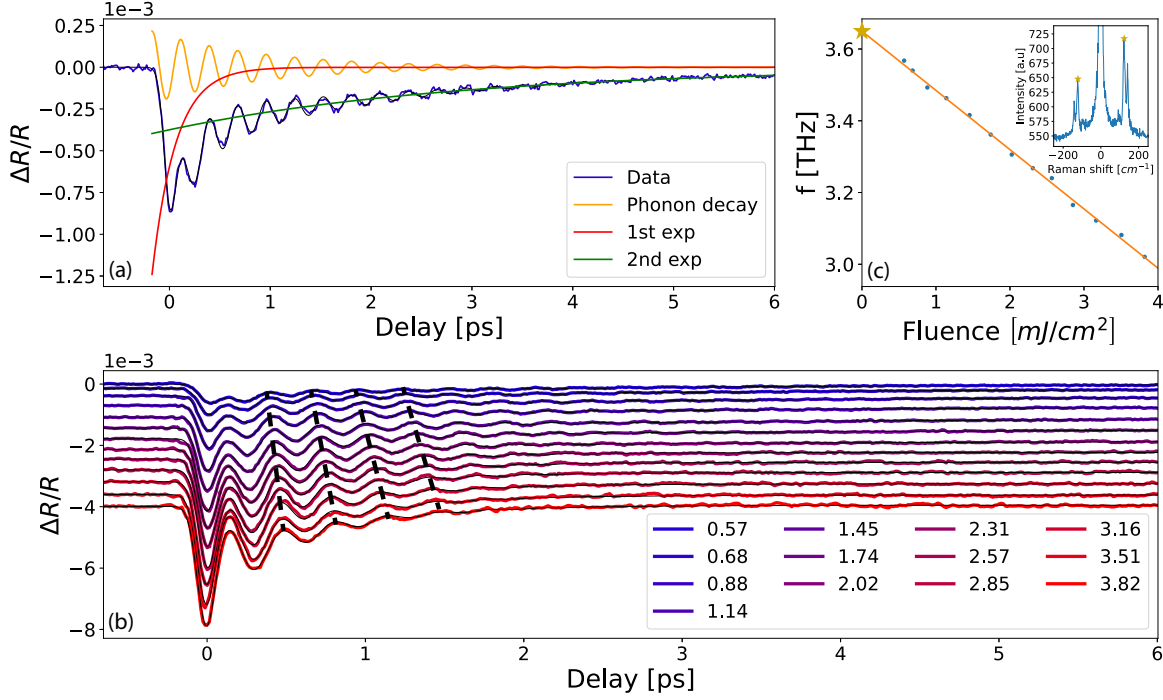


Figure 1: (a) $\Delta R/R$ of SnTe with an incident pump fluence of $0.684 [mJ/cm^2]$. The blue line is the data, and the black curve is its fit. The red, green, and yellow solid lines are the decomposition of the fit to its exponential and oscillatory components. (b) Fluence dependence of the $\Delta R/R$. Data is shown in color, and fits are shown as thin black lines. The dashed black lines are guides to the eye through the oscillatory peaks. Data is vertically shifted for clarity. Incident fluences are specified in units of mJ/cm^2 . (c) Frequencies extracted from the fits to the data shown in panel (b) as a function of the applied pump fluence. The star marks the frequency measured by Raman scattering. In the inset, Raman scattering measurement. A star marks the Stokes and anti-Stokes peaks corresponding to the same mode measured using the pump-probe technique.

Optical phonon softening as a result of increasing laser fluence was observed in several compounds in the past²⁷⁻³¹. The most relevant example for our work is SnSe where the phonon softening was associated with softening of the $Se4p_x - Sn5s$ bond due to the photo-excitation of

electrons²⁷. Similar phenomena were also observed in bismuth where the nature of the phonon softening, whether electronic or anharmonic, was debated in a series of papers^{28–30}. From these examples alone, it is clear that phonon softening as a function of the laser fluence can originate from various sources. This is due to the multitude of effects that occur when the pump pulse interacts with the sample, including heating, photo-excitation of electrons, and the excitation of coherent phonons. Ideally, one would isolate the contributions of the different effects by tuning them individually. While this is possible for infrared active modes via resonant excitation^{32–35} it is a very challenging task for the amplitude Raman active modes since their excitation is typically a non-resonant process such as DECP²³ which inherently involves an electronic excitation or a sudden temperature increase. Two unique cases are the experiments by Maehrlein et al³⁶ and Giorgianni et al³⁷ who were able to resonantly pump a Raman active phonons in diamond and V₂O₃ respectively by using sum frequency of two low energy phonons in the mid-infrared and THz regimes respectively. In the case of diamond this was made possible thanks to the very high frequency (40 THz) of the particular mode and its unusually high Raman activity and for the case of V₂O₃ it was made possible thanks to a very strong THz field and similarly strong Raman activity. A double pump experiment by Murry et al³⁰ shows that in bismuth fluence dependent softening originates from the coupling of the A_{1g} phonon to the electron-hole plasma by showing that the phonon frequency does not change as a function of the pump-pump delay. In our experiment, we go beyond what was previously demonstrated and show that the distinct transient characteristics of structural, electronic, and thermal effects serve as unique fingerprints to isolate their impacts on phonon anharmonicity using double pump-probe spectroscopy.

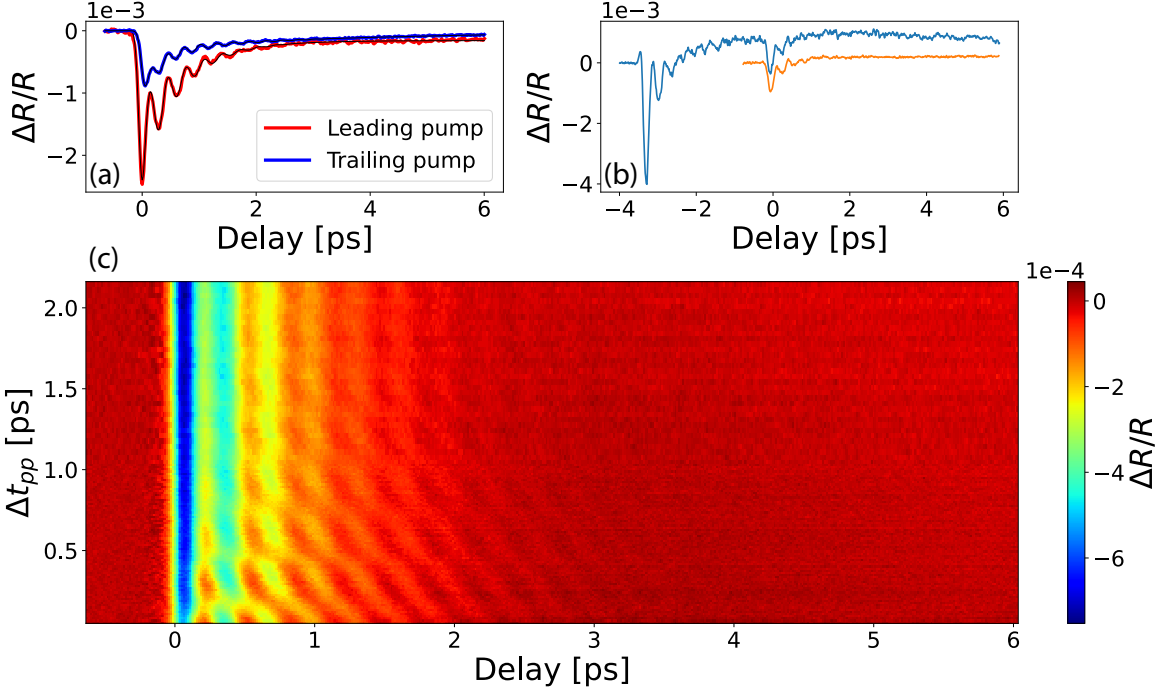


Figure 2: (a) $\Delta R/R$ data taken with single pump excitation. The blue curve is taken only with the trailing pump whereas the red curve is taken only with the leading pump. (b) $\Delta R/R$ data taken with both pumps incident on the sample with $\Delta t_{pp} = 3.31[\text{ps}]$. The blue curve was taken with the chopper modulating both pump beams and the orange curve corresponds to a measurement in which only the trailing pump is modulated by the chopper. (c) Color map of the double pump $\Delta R/R$ data. Colors represent the magnitude of $\Delta R/R$, the horizontal axis is the time delay between the probe and the trailing pump whereas the vertical axis is Δt_{pp} .

The incident fluences of the two pump beams were set to $2.822[\text{mJ}/\text{cm}^2]$ for the leading pump and $0.571[\text{mJ}/\text{cm}^2]$ for the trailing pump. These correspond to excitation densities of $\approx 1.840 \times 10^{22}$ and $3.72 \times 10^{21}[\text{cm}^{-3}]$ respectively. Their respective single pump $\Delta R/R$ traces are shown in Figure 2(a). The observed frequencies are 3.14 THz and 3.48 THz, corresponding to the pulses that will act as leading and trailing pump pulses in the double pump-probe experiment.

Our optical setup allows us to isolate the portion of $\Delta R/R$ originating from the trailing pump by modulating it with a mechanical chopper. The efficiency of the isolation process is demonstrated in Figure 2(b). The time delay between the two pump pulses (Δt_{pp}) was set to 3.31 ps, and the arrival time of the probe pulse was scanned relative to the two pump pulses. The blue trace shows the measurement when the chopper modulates both pump pulses, whereas the orange trace shows the measurement where only the trailing pump was. The measurement was repeated for different values of Δt_{pp} and the results are shown in Figure 2(c). The oscillation frequency of $\Delta R/R$ changes with Δt_{pp} , as could be seen by the horizontal shift of the oscillation peaks. However, in contrast to the monotonically increasing mode softening, which was observed as a function of laser fluence (Figure 1), a nonmonotonic oscillatory behavior as a function of Δt_{pp} is observed.

To closely examine the origin of the nonmonotonic behavior, we plot in Figure 3 the frequency of the oscillations as a function of Δt_{pp} (detailed analysis in supplementary section 3). Figure 3(a) focuses on the long timescale features in the data. Significant softening is observed which follows a double exponential behavior as a function of Δt_{pp} with amplitudes and time constants of $A_1 = -0.23[THz]$, $\tau_1 = 3.87[ps]$, $A_2 = -0.10[THz]$, $\tau_2 = 155[ps]$. The long timescale of the second exponent is characteristic of thermal relaxation and we therefore attribute this contribution to quasi-harmonic effects³⁸ induced by the heating of the leading pump. The fast exponent is characteristic of electronic relaxation and is related to the relaxation of the photo-excited electrons back to their original states. This timescale is comparable to electronic relaxation timescales measured in the past by time-resolved photo-emission spectroscopy²⁵. The softening characteristic of the electronic feature is expected since we know that photo-excitation acts to soften the chem-

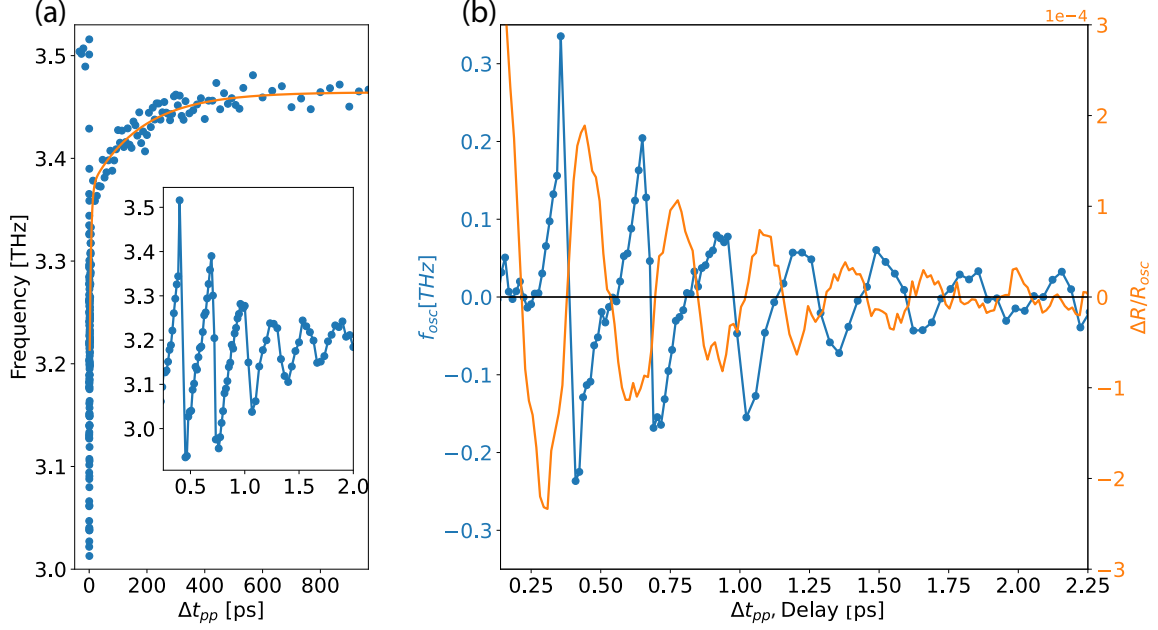


Figure 3: (a) Phonon frequency as a function of Δt_{pp} . The inset shows a magnification for small values of Δt_{pp} . (b) The blue curve shows the oscillatory component of the data in (a) for which the horizontal axis represents Δt_{pp} . The orange curve is the oscillatory component of $\Delta R/R$ of the leading pump for which the horizontal axis represents the time delay between the pump and probe pulses.

ical bonds between the Te anions and Sn cations. Moreover, it is compatible with the behavior calculated and observed in the sister compound SnSe²⁷. Figure 3(b) focuses on short timescales of the Δt_{pp} and shows a distinct periodic non-sinusoidal behavior. The oscillatory component of the $\Delta R/R$ trace obtained when only the leading pump was incident on the sample is plotted for comparison. The periods and time constants of both signals match, indicating that the periodic component of the frequency shift is caused by displacing the atoms along the A_g normal coordinate serving as a direct measurement for the modes anharmonicity. The magnitude of the oscillations

reaches values as large as 0.3[THz] which is larger than both the thermal and the electronic effects. Moreover, this value is larger than what was observed for a similar value of the fluence in the single pump experiment. The sign of the periodic signal is correlated with that of the sinusoidal component of the $\Delta R/R$ signal. A positive $\Delta R/R$ and extension of the mode is accompanied by phonon softening while a negative $\Delta R/R$ is accompanied by hardening and contraction of the mode. This is in agreement with our previous understanding (Figure 1) that the softening of the mode is correlated with a positive sign of the oscillations at time zero where the DECP process acts to extend the mode. The periodic signal is asymmetric between its rising and descending parts. The rising side is slow, smooth, and seems to have an inflection point at the times where the $\Delta R/R$ signal crosses zero. In contrast, the descending part is sharp, and its exact features are beyond our experimental resolution which is limited by the duration of the two pump pulses. The asymmetry between the rising and descending parts of the data indicates that it is not only the position of the atoms along the phonon coordinate that determines the observed frequency but also the direction of their momentum at the time of photo-excitation. The origin of symmetry breaking is the directional nature of the DECP process, i.e., mode extension accompanied by softening. Similar asymmetric line-shapes were observed in the phase of coherent phonons in diamond²² and in the phonon lifetime in bismuth³⁹ which were also excited using the DECP process. We note that while the similar line-shapes are characteristic of the DECP process, lattice anharmonicity was not observed in either bismuth or diamond. Similar measurements were taken using different fluences for the leading and trailing pump pulses. The full datasets and their analysis are provided in supplementary section 5 and show similar results. The signals vary in their amplitude and charac-

teristic timescales which demonstrates the potential of the double pump method to control material properties.

SnTe has the rocksalt structure, therefore its fully symmetric A_g mode is similar to a uniform expansion of the crystal which also happens as a function of increased temperature. Therefore, the observed changes in frequency could be thought of as the coherent and thermal versions of the lattice expansion effect. To test whether the double pump method can identify anharmonicity along less symmetric phonon modes we performed similar measurements on SnSe, a low-symmetry variant of SnTe. Figure 4(a) shows the $\Delta R/R$ signal taken with single pump excitation. It is clear from the beat-like pattern, that more than a single frequency is present in the signal corresponding to more than one phonon in agreement with previous measurements of SnSe²⁷. Figure 4(b) shows $\Delta R/R$ as a function of time delay and Δt_{pp} . Unlike in Figure 2(b), the presence of multiple frequencies in the data makes it challenging to decipher the anharmonic effects directly from the plot. To decrease the amount of fitting parameters we first subtract the exponential background and fit the data to a combination of damped oscillations to extract the mode frequencies as a function of Δt_{pp} . The results for the two most dominant phonons are shown in Figure 4 (c-d). Both modes were observed previously in single pump experiments²⁷ and are known to soften with increased fluence. However, as Δt_{pp} is increased both modes exhibit periodic modulations at the frequency excited by the leading pump for the same mode. In contrast to SnTe, the lower symmetry of SnSe differentiates between lattice expansion and motion along the crystals A_g modes, and Huang et.al²⁷ even showed that their excitation is entwined with a novel lattice instability towards a higher symmetry phase.

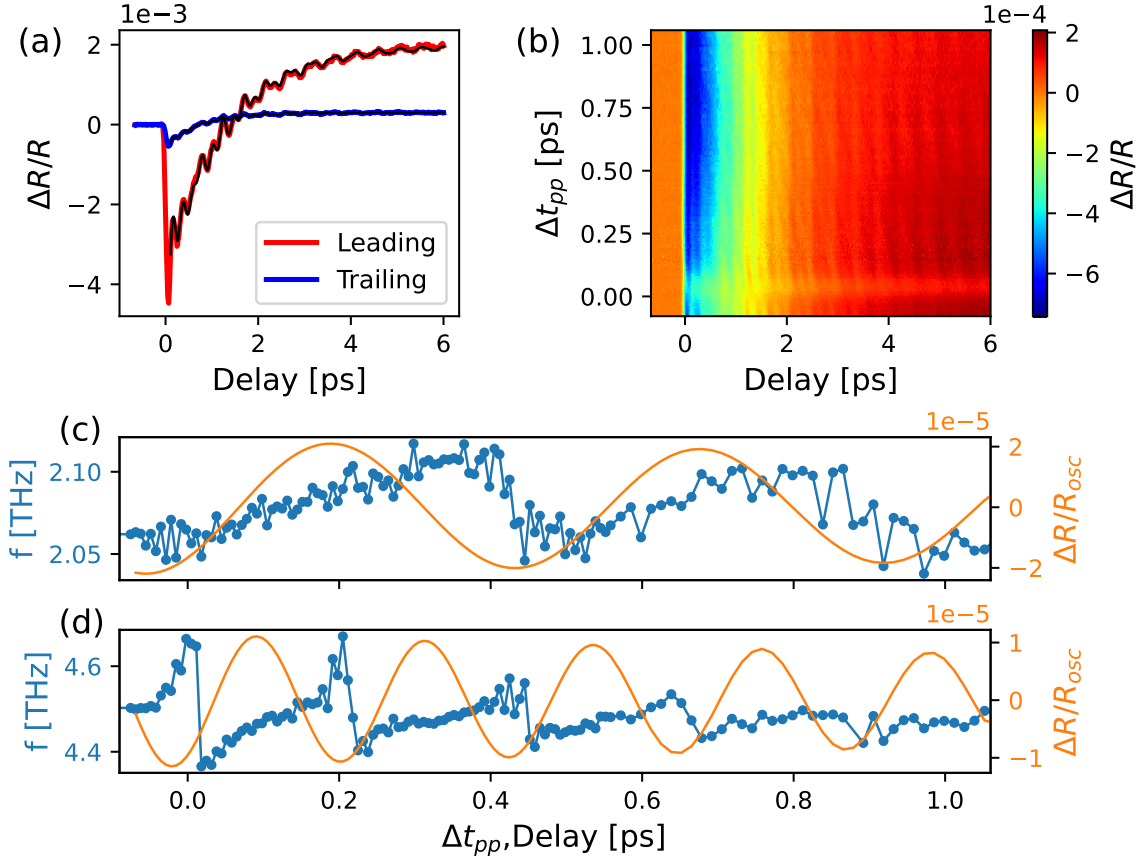


Figure 4: (a) $\Delta R/R$ data in SnSe, taken with single pump excitation. The blue curve is taken only with the trailing pump whereas the red curve is taken only with the leading pump. (b) Color map of the double pump $\Delta R/R$ data for SnSe. Colors represent the magnitude of $\Delta R/R$, the horizontal axis is the time delay between the probe and the trailing pump whereas the vertical axis is Δt_{pp} . In panels (c) and (d), similar plots to that presented in Figure 3(b) are presented, corresponding to two of the A_g phonons of SnSe. In both panels, the blue curves show the phonons' frequency as a function of Δt_{pp} and the orange curves are the corresponding oscillatory component of $\Delta R/R$ of the leading pump, which were extracted by fitting to the pump-probe data shown in panel (a), as a function of the time delay between the pump and the probe pulses.

Our experiment serves as a direct measurement of the anharmonicity of a single phonon mode originating from deviations from the parabolic shape of the potential for the ions. This is in contrast to line broadening and coherent coupling between different modes which are typically used to characterize anharmonicity. Our study demonstrates that double pump-probe spectroscopy is a powerful tool for disentangling the thermal, electronic, and anharmonic contributions to phonon frequency shifts. By applying this technique, we have been able to gain detailed insights into the complex interplay of these factors in SnTe and SnSe. Importantly, the applicability of our approach to disentangling electronic from thermal effects in ultrafast measurements is broader than the application discussed here. For example, light-induced phase transitions are tuned as a function of the pump fluence⁴⁰. In many cases the nature of the transition, whether of thermal or electronic origins is debated. Typically, a theoretical understanding of the particular system at hand is required in addition to the experimental data to reach a definitive conclusion. We show that the double pump technique separates between thermal and electronic effects by their distinct temporal behavior and can greatly aid in solving these debates.

Methods SnTe single crystals were grown using the vapor transport technique without the aid of a transport agent similar to the procedure described in Ref⁴¹. Stoichiometric amounts of Sn(99.995% Sigma Aldrich) and Te(99.999% Thermoscientific) were weighed and thoroughly mixed inside an alumina crucible. The starting materials were sealed under vacuum in a 20 cm long quartz ampule which was placed in a gradient tube furnace. The starting materials were positioned in the hot zone of the furnace. The source and growth zones of the furnace were ramped to 797°C and 747°C respectively at a rate of 25°C/hour. The synthesis took place for 1 week after which large single crystals were found in the cold zone of the tube. A similar procedure was used to grow SnSe. Selected crystals were ground to a fine powder using a mortar and pestle which was used to characterize the structure of the crystals using powder X-ray diffraction (see supplementary section 2).

Detailed information about the optical experiment, not provided in the main text, is shown in supplementary section 1.

Acknowledgements A.R. acknowledges support from the Zuckerman Foundation, and the Israel Science Foundation (Grant No. 1017/20). This research was supported by the Ministry of Innovation, Science and Technology, Israel. Gili Scharf acknowledges support from the Israeli Clore fellowship.

Data availability The data that support the findings of this study are available from the corresponding author upon reasonable request.

Author contribution All authors contributed to the production of this manuscript.

Competing Interests The authors declare no competing financial interests.

Correspondence Correspondence and requests for materials should be addressed to Alon Ron (email:

alonron@tauex.tau.ac.il).

1. Delaire, O. *et al.* Giant anharmonic phonon scattering in pbte. *Nature materials* **10**, 614–619 (2011).
2. Wei, B., Sun, Q., Li, C. & Hong, J. Phonon anharmonicity: a pertinent review of recent progress and perspective. *Science China Physics, Mechanics & Astronomy* **64**, 117001 (2021).
3. Knoop, F., Purcell, T. A., Scheffler, M. & Carbogno, C. Anharmonicity in thermal insulators: An analysis from first principles. *Physical Review Letters* **130**, 236301 (2023).
4. Wallace, D. C. Thermal expansion and other anharmonic properties of crystals. *Physical Review* **139**, A877 (1965).
5. Budai, J. D. *et al.* Metallization of vanadium dioxide driven by large phonon entropy. *Nature* **515**, 535–539 (2014).
6. Teitelbaum, S. W. *et al.* Direct measurement of anharmonic decay channels of a coherent phonon. *Physical review letters* **121**, 125901 (2018).
7. Golonzka, O., Khalil, M., Demirdöven, N. & Tokmakoff, A. Coupling and orientation between anharmonic vibrations characterized with two-dimensional infrared vibrational echo spectroscopy. *The Journal of Chemical Physics* **115**, 10814–10828 (2001).
8. Fulmer, E. C., Mukherjee, P., Krummel, A. T. & Zanni, M. T. A pulse sequence for directly measuring the anharmonicities of coupled vibrations: Two-quantum two-dimensional infrared spectroscopy. *The Journal of chemical physics* **120**, 8067–8078 (2004).

9. Golonzka, O., Khalil, M., Demirdöven, N. & Tokmakoff, A. Vibrational anharmonicities revealed by coherent two-dimensional infrared spectroscopy. *Physical review letters* **86**, 2154 (2001).
10. Lin, H.-W., Mead, G. & Blake, G. A. Mapping linbo 3 phonon-polariton nonlinearities with 2d thz-thz-raman spectroscopy. *Physical Review Letters* **129**, 207401 (2022).
11. Först, M. *et al.* Nonlinear phononics as an ultrafast route to lattice control. *Nature Physics* **7**, 854–856 (2011).
12. Toberer, E. S., Zevalkink, A. & Snyder, G. J. Phonon engineering through crystal chemistry. *Journal of Materials Chemistry* **21**, 15843–15852 (2011).
13. Brebrick, R. & Strauss, A. Anomalous thermoelectric power as evidence for two-valence bands in snTe. *Physical Review* **131**, 104 (1963).
14. Li, C. *et al.* Phonon self-energy and origin of anomalous neutron scattering spectra in snTe and pbTe thermoelectrics. *Physical review letters* **112**, 175501 (2014).
15. Lee, S. *et al.* Resonant bonding leads to low lattice thermal conductivity. *Nature communications* **5**, 3525 (2014).
16. Ribeiro, G. A. *et al.* Strong anharmonicity in the phonon spectra of pbTe and snTe from first principles. *Physical Review B* **97**, 014306 (2018).
17. Hsieh, T. H. *et al.* Topological crystalline insulators in the snTe material class. *Nature communications* **3**, 982 (2012).

18. Johnson, A. S. *et al.* All-optical seeding of a light-induced phase transition with correlated disorder. *Nature Physics* 1–6 (2024).
19. Horstmann, J. G. *et al.* Coherent control of a surface structural phase transition. *Nature* **583**, 232–236 (2020).
20. Maklar, J. *et al.* Coherent light control of a metastable hidden state. *Science Advances* **9**, eadi4661 (2023).
21. Hu, J., Igarashi, K., Sasagawa, T., Nakamura, K. G. & Misochko, O. V. Femtosecond study of a1g phonons in the strong 3d topological insulators: From pump-probe to coherent control. *Applied Physics Letters* **112** (2018).
22. Sasaki, H. *et al.* Coherent control theory and experiment of optical phonons in diamond. *Scientific Reports* **8**, 9609 (2018).
23. Vidal, J. *et al.* Displacive excitation of coherent phonons. In *International Conference on Ultrafast Phenomena*, ThC2 (Optica Publishing Group, 1992).
24. Suzuki, N. & Sadao Adachi, S. A. Optical properties of snte. *Japanese Journal of Applied Physics* **34**, 5977 (1995). URL <https://dx.doi.org/10.1143/JJAP.34.5977>.
25. Ito, H. *et al.* Observation of unoccupied states of snte (111) using pump-probe arpes measurement. *Physical Review Research* **2**, 043120 (2020).
26. Su, Y. *et al.* Orietation-controlled synthesis and raman study of 2d snte. *Nanotechnology* **34**, 505206 (2023).

27. Huang, Y. *et al.* Observation of a novel lattice instability in ultrafast photoexcited sncse. *Physical Review X* **12**, 011029 (2022).
28. Hase, M., Kitajima, M., Nakashima, S.-i. & Mizoguchi, K. Dynamics of coherent anharmonic phonons in bismuth using high density photoexcitation. *Physical review letters* **88**, 067401 (2002).
29. Fritz, D. M. *et al.* Ultrafast bond softening in bismuth: Mapping a solid's interatomic potential with x-rays. *Science* **315**, 633–636 (2007).
30. Murray, E., Fritz, D., Wahlstrand, J., Fahy, S. & Reis, D. Effect of lattice anharmonicity on high-amplitude phonon dynamics in photoexcited bismuth. *Physical Review B—Condensed Matter and Materials Physics* **72**, 060301 (2005).
31. He, B. *et al.* Coherent optical phonon oscillation and possible electronic softening in wte2 crystals. *Scientific Reports* **6**, 30487 (2016).
32. Katayama, I. *et al.* Ferroelectric soft mode in a strto 3 thin film impulsively driven to the anharmonic regime using intense picosecond terahertz pulses. *Physical review letters* **108**, 097401 (2012).
33. von Hoegen, A., Mankowsky, R., Fechner, M., Först, M. & Cavalleri, A. Probing the interatomic potential of solids with strong-field nonlinear phononics. *Nature* **555**, 79–82 (2018).
34. Melnikov, A., Selivanov, Y. G. & Chekalin, S. Anharmonic coherent dynamics of the soft phonon mode of a pbte crystal. *Physical Review B* **108**, 224309 (2023).

35. Xu, C. & Zong, A. Time-domain study of coupled collective excitations in quantum materials. *npj Quantum Materials* **10**, 21 (2025).
36. Maehrlein, S., Paarmann, A., Wolf, M. & Kampfrath, T. Terahertz sum-frequency excitation of a raman-active phonon. *Physical review letters* **119**, 127402 (2017).
37. Giorgianni, F. *et al.* Terahertz displacive excitation of a coherent raman-active phonon in v2o3. *Communications Physics* **5**, 103 (2022).
38. Walsh, A. & Watson, G. W. Influence of the anion on lone pair formation in sn (ii) monochalcogenides: A dft study. *The Journal of Physical Chemistry B* **109**, 18868–18875 (2005).
39. Cheng, Y.-H., Gao, F. Y., Teitelbaum, S. W. & Nelson, K. A. Coherent control of optical phonons in bismuth. *Physical Review B* **96**, 134302 (2017).
40. de la Torre, A. *et al.* Decoupling of static and dynamic criticality in a driven mott insulator. *Communications Physics* **5**, 35 (2022).
41. Kannaujiya, R. M. *et al.* Growth and characterizations of tin telluride (snte) single crystals. *The European Physical Journal Plus* **135**, 1–12 (2020).
42. Beattie, A. Temperature dependence of the elastic constants of tin telluride. *Journal of Applied Physics* **40**, 4818–4821 (1969).
43. Zhou, M. *et al.* Optimization of thermoelectric efficiency in snte: the case for the light band. *Phys. Chem. Chem. Phys.* **16**, 20741–20748 (2014). URL <http://dx.doi.org/10.1039/C4CP02091J>.

44. Damon, D. Thermal conductivity of snse between 100 and 500 k. *Journal of Applied Physics* **37**, 3181–3190 (1966).
45. Barrios-Salgado, E., Nair, M. & Nair, P. Chemically deposited snse thin films: thermal stability and solar cell application. *ECS Journal of Solid State Science and Technology* **3**, Q169 (2014).

Supplemental Material for: "Coherent control through phonon anharmonicity"

Gili Scharf¹, Tomer Hasharoni¹, Lara Donval¹, Leah Ben Gur¹, Alon Ron¹

¹*Raymond and Beverly Sackler School of Physics and Astronomy, Tel-Aviv 69978, Israel*

1 Optical setup

This section describes the optical setup used to take the single and double pump probe measurements. 1030 nm pulses were generated by a regenerative amplifier at a repetition rate of 50 kHz, these were used to pump a pair of optical parametric amplifiers seeded by the same white light crystal. The wavelength of the signal beams of the two optical parametric amplifiers were set to 750 nm and 800 nm and were used as pump and probe respectively. For the single pump experiments, the fluence of the probe did not change throughout the experiment and was set to $20[\mu J/cm^2]$, that of the pump beams was varied as described in the main text. The pump beam was split by a 50:50 beamsplitter. The pump beam was modulated at a frequency of 5 kHz in one of two possible positions before and after the beamsplitter for isolation of the signal originating from the trailing pump beam as described in the main text. The pumps' intensities were varied by using neutral density filters.

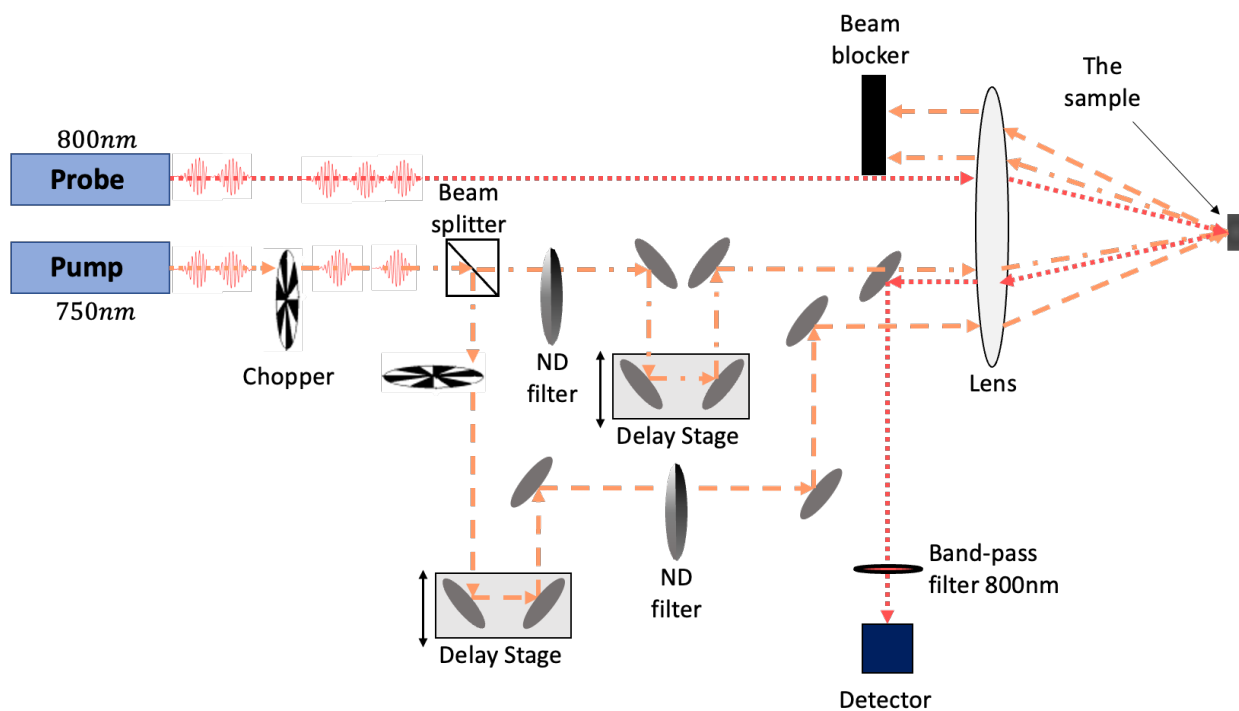


Figure S1: Schematic of the optical setup used in this work. Unlabeled components are silver mirrors.

2 X-ray diffraction

In this section, we show the X-ray diffraction data of SnTe and SnSe powders taken from the same batches as the crystals used for the optical experiments. The crystals were ground to powder using an agate mortar and pestle before the measurements. All observable peaks were associated with peaks expected for the known phases of SnTe and SnSe using Rietveld refinement. Figure S2 shows the measured diffraction patterns taken using a Cu $k\alpha$ source. All peaks in the pattern agree with the expected peak positions of the known phases and weak peaks are not marked for clarity. A polynomial background was subtracted from the SnSe data.

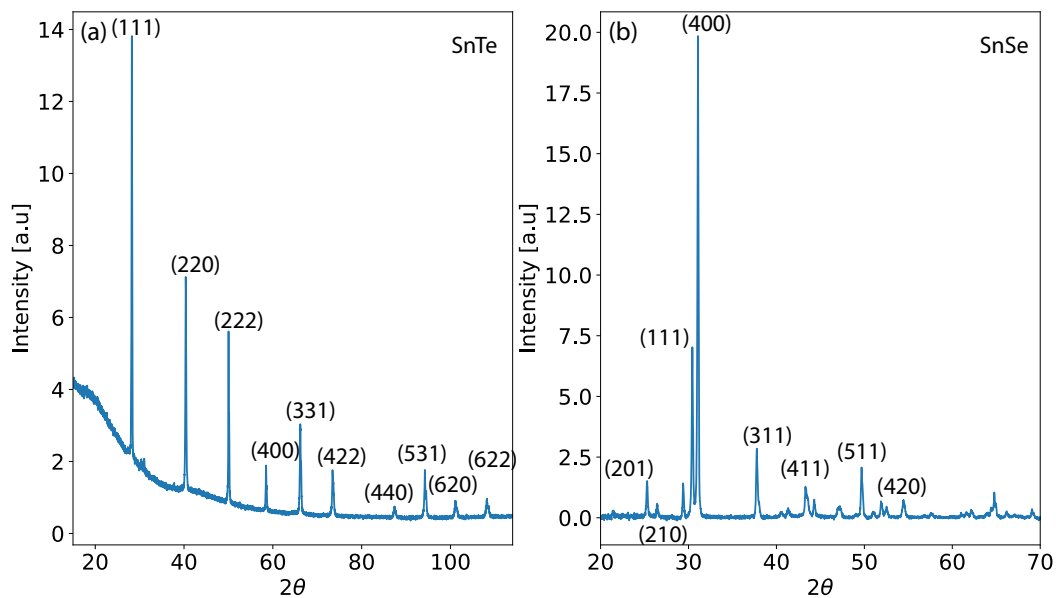


Figure S2: Powder X-ray diffraction data of (a) SnTe and (b) SnSe samples are presented. Miller indices are displayed next to the main observed peaks. For SnSe, a polynomial background was subtracted from the data.

3 Detailed analysis

Analysis of the data shown in Figure 3 in the main text was performed in the following way. A high pass filter with a cutoff frequency of 2 THz was first applied to the data. The oscillatory component was fit according to the following expression:

$$Ae^{-t/\tau} \cos(\omega t + \phi) + c. \quad (1)$$

The final results of this analysis procedure are shown in Figure 3 of the main text. In the following paragraph, we provide a detailed analysis on a portion of the data. Figure S3(a) shows the same result as plotted in the main text Figure 3(b) with one distinction. A subset of the data is highlighted in green and its detailed analysis is presented in this section. Figure S3(b) shows the raw data shifted for clarity for the range Δt_{pp} between 0.4 to 0.65[ps]. The red dots in Figure S3(c) show the same data after the application of a high-pass filter with a cutoff frequency of 2 THz. The numbers to the right of panel (c) are values of Δt_{pp} corresponding to the data near them in ps. The black lines show fits to the data according to supplementary equation 1. As can be seen, the expression fits the data nicely for all values of Δt_{pp} .

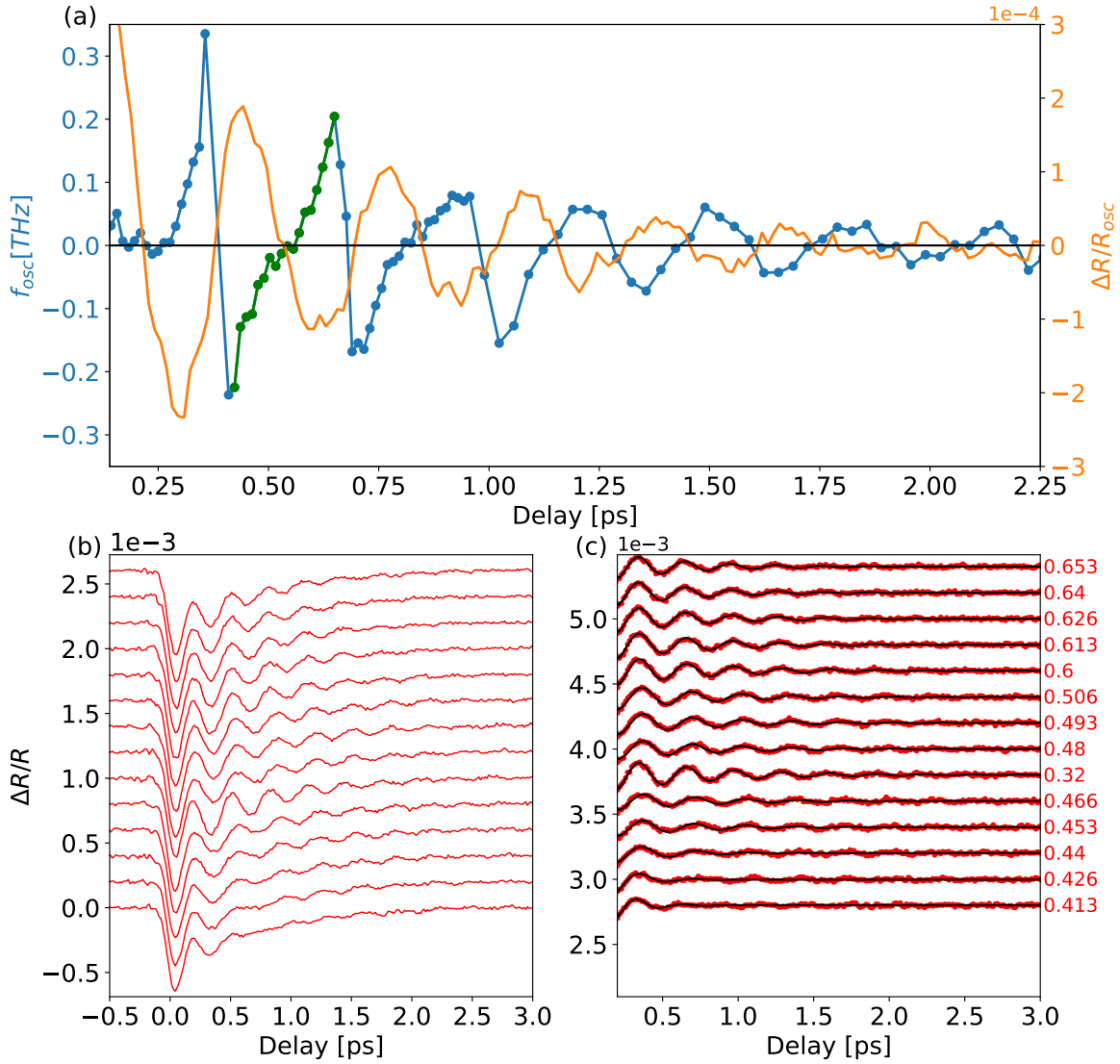


Figure S3: (a) Same data as in Figure 3(b) in the main text. A detailed analysis for the points highlighted in green is presented in panels (b,c). (b) Raw data vertically shifted for clarity. Values of Δt_{pp} are the same as the corresponding traces in panel (c). (c) The data in (b) after the application of a high pass filter with a cutoff frequency at 2 THz. The numbers to the right of the panel correspond to the values of Δt_{pp} in ps. Black lines are the fit results to equation (1).

4 Estimation of the thermal time constant

We estimate the thermal time constant by:

$$\tau_{thermal} = R_{thermal} \cdot C_{thermal} \quad (2)$$

where $R_{thermal}$ and $C_{thermal}$ are the thermal resistance and heat capacity of the probed volume, respectively. We can express the $R_{thermal}$ in the following manner:

$$\rho_{thermal} = 1/\kappa = R_{thermal} \frac{A}{l} \Rightarrow R_{thermal} = \frac{l}{A \cdot \kappa} \quad (3)$$

where $\rho_{thermal}$, the thermal resistivity, is the inverse of κ , the thermal conductivity, A is the surface area of the incident probe beam and l is the penetration depth of the probe. The heat capacity can be expressed as the heat capacity per unit mass, $c_{thermal}$, multiplied by M , the mass of the volume irradiated by the probe beam:

$$C_{thermal} = c_{thermal} \cdot M = c_{thermal} \cdot \rho \cdot V = c_{thermal} \cdot \rho \cdot A \cdot l \quad (4)$$

The penetration depth of the probe, which is the inverse of the attenuation constant (α), is determined by the wavelength of the probe (λ) and the imaginary part of the complex refracting index ($\tilde{n}(\lambda)$):

$$l = \frac{1}{\alpha} = \left(\frac{4\pi}{\lambda} \cdot \Im[\tilde{n}(\lambda)] \right)^{-1} \quad (5)$$

Combining all of the above and using values from literature^{24,42-44} gives $\tau_{thermal} \sim 25.02$ ps.

5 Double pump measurements of SnTe with additional fluences

The main text presents double pump measurements of SnTe at a single combination of fluences. In this section, we show two additional datasets, the first with incident fluences of 1.454 and 0.708[mJ/cm²] (corresponding to excitation densities of $\approx 9.48 \times 10^{21}$ and 4.62×10^{21} [cm⁻³])²⁴ for the leading and trailing pump beams respectively, and the second with incident fluences of 3.51 and 0.777[mJ/cm²] (which correspond to excitation densities of $\approx 2.286 \times 10^{22}$ and 5.06×10^{21} [cm⁻³])²⁴. The measurements show qualitatively similar results to those shown in the main text. The main difference is that the frequency of modulations shown in Figures S4(c) and Figure S5(c) are different than the frequency presented in the main text. In all cases it corresponds to the frequency of the phonon observed when using only the leading pump.

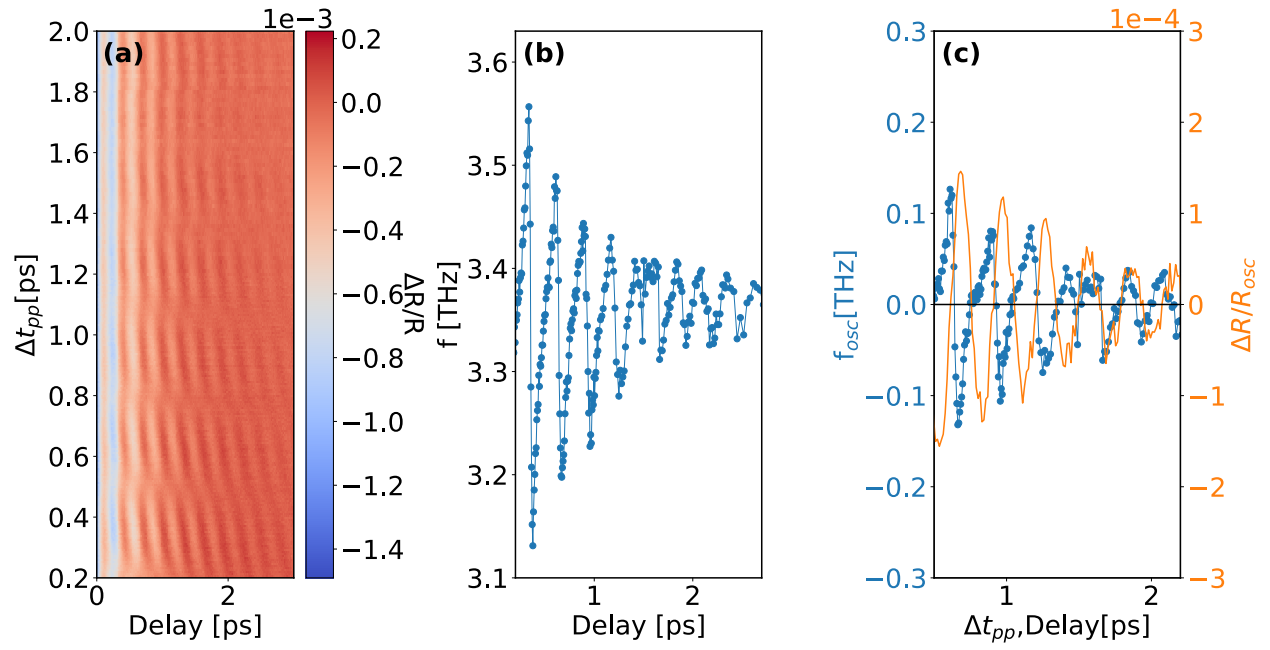


Figure S4: (a) Colormap showing $\Delta R/R$ as a function of delay time and Δt_{pp} for incident fluences of 1.454 and 0.708 [mJ/cm^2]. (b) The extracted phonon frequencies as a function of Δt_{pp} . (c) The blue curve shows the oscillatory component of the measured frequencies as a function of Δt_{pp} . The overlaid orange curve shows the oscillatory component of $\Delta R/R$ measured using only the leading pump.

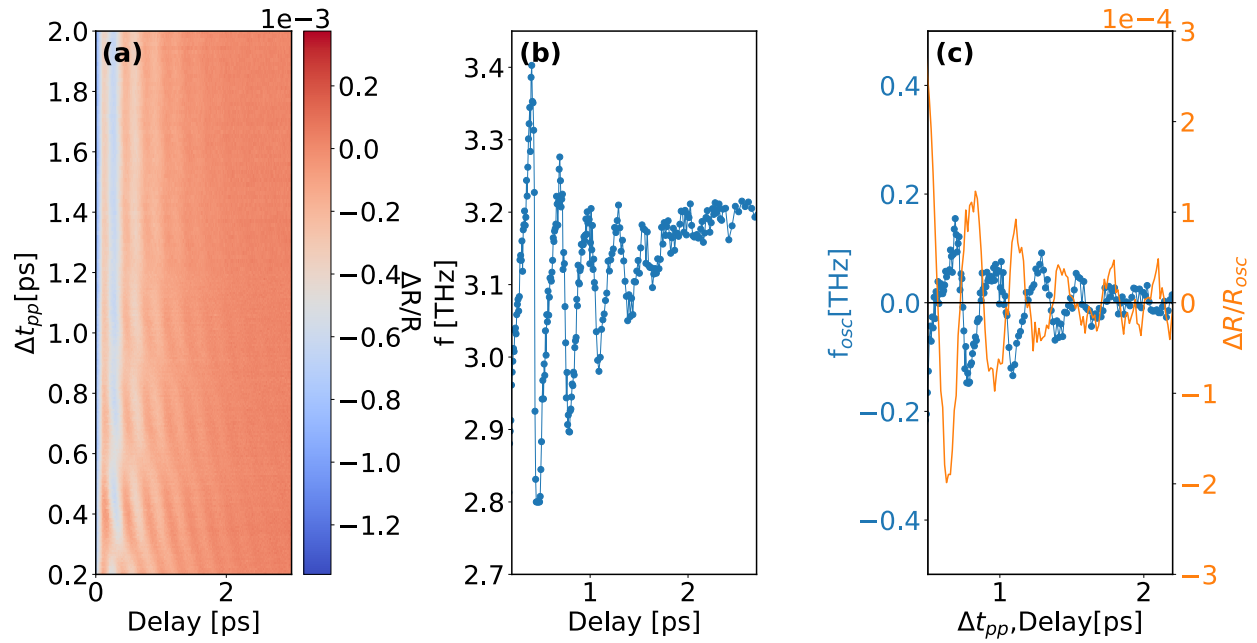


Figure S5: (a) Colormap showing $\Delta R/R$ as a function of delay time and Δt_{pp} for incident fluences of 3.51 and 0.777 [mJ/cm^2]. (b) The extracted phonon frequencies as a function of Δt_{pp} . (c) The blue curve shows the oscillatory component of the measured frequencies as a function of Δt_{pp} . The overlaid orange curve shows the oscillatory component of $\Delta R/R$ measured using only the leading pump.

6 Simulation of chirped phonon and comparison to a non-chirped phonon for SnTe

In this section, we show that frequency modulations in the phonon frequency of SnTe are undetectable due to the short lifetime of the phonon and that if present, changes to the resulting values will be within the error of the central frequencies reported. We simulate exponentially decaying oscillatory time series with central frequencies similar to those measured in our experiment. We add frequency modulation according to the equation shown in the figure legend. The values for the magnitude of the modulation are taken from the experimental results shown in the main text Figure 3(b) and in the supplementary, Figure S4(c). The similarity of the modulated signal to the non-modulated signal is clear from the good agreement between them as seen in Figures S6 and S7. Any visible discrepancies are comparable to the magnitude of our experimental measurement error. This means that under these conditions, modulations to the central frequency (such as chirp) are undetectable in our experiment and, if present in SnTe.

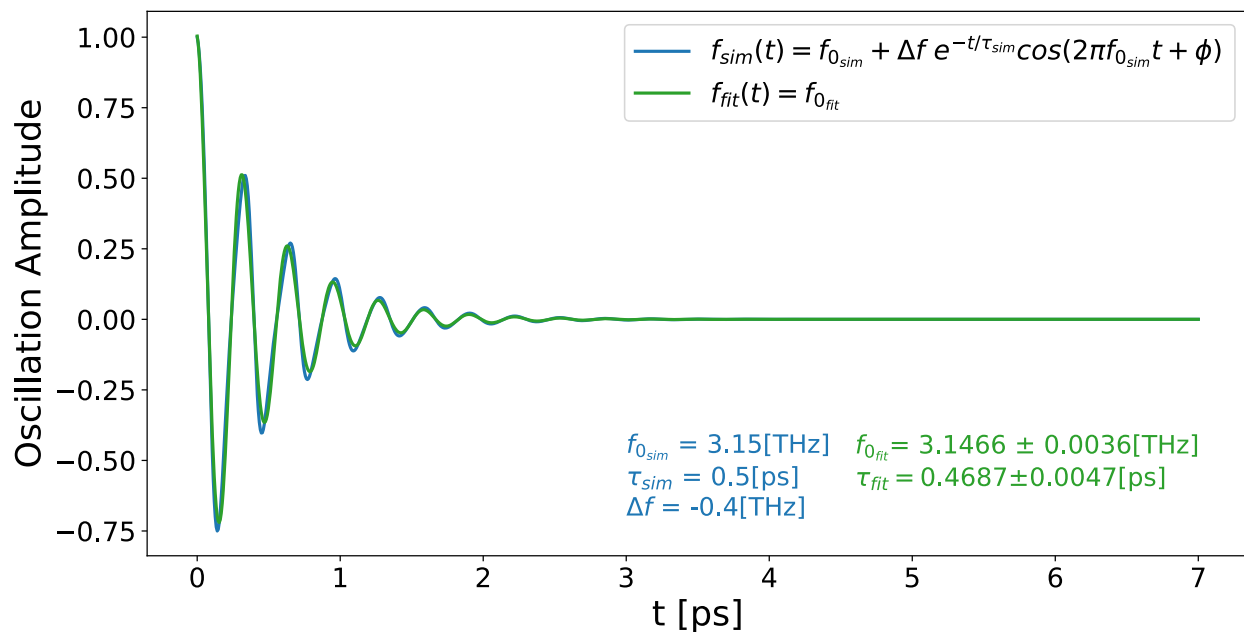


Figure S6: A simulation of a phonon decay with a frequency time-dependency of $f(t) = f_0 + \Delta f e^{-t/\tau} \cos(2\pi f_0 t + \phi)$ is shown in blue. For the simulation, f_0 and τ were selected to be the values from the fit to the pump-probe data of the leading pump, shown in Figure 2(a) in the main text, ϕ was taken to be 0, and Δf was determined using Figure 3(b) in the main text. All these values (ϕ was set to 0), are shown in the figure in blue. In green, we show a fit to the simulated data without accounting for any frequency modulation. The resulting frequency and time-decay are shown in the figure in green.

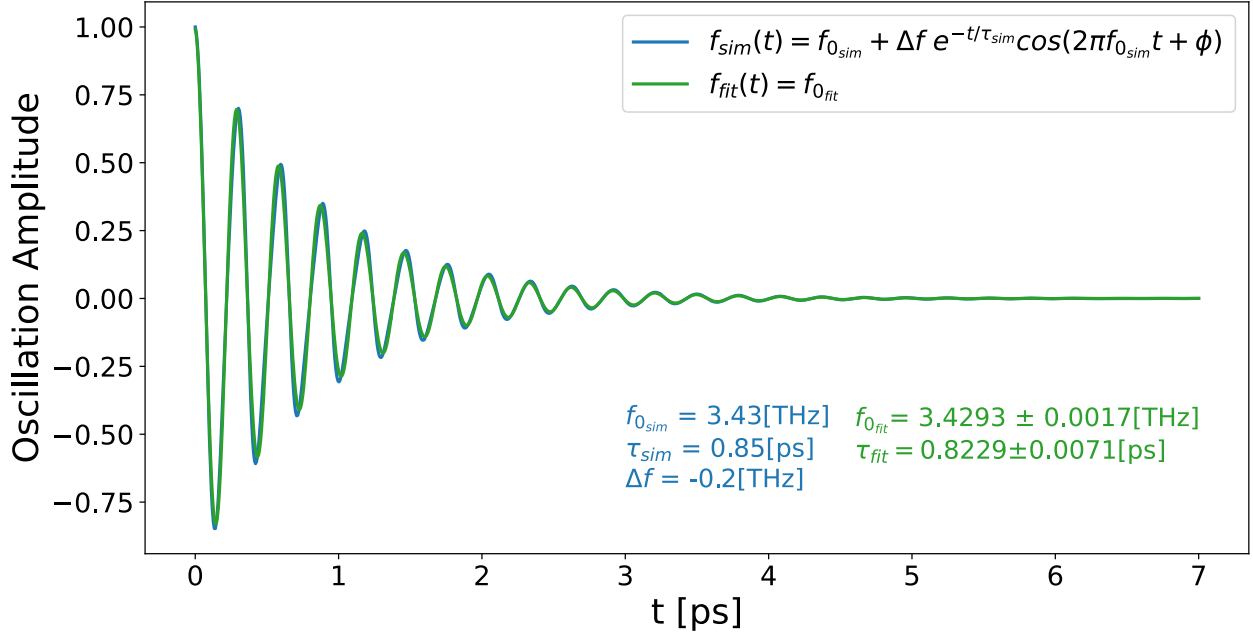


Figure S7: A simulation of a phonon decay with a frequency time-dependency of $f(t) = f_0 + \Delta f e^{-t/\tau} \cos(2\pi f_0 t + \phi)$ is shown in blue. For the simulation, f_0 and τ were taken as the experimental values from the pump-probe data with leading pump fluence of $1.454[mJ/cm^2]$, ϕ was set to zero, and Δf was determined using Figure S4(c) in the main text. All these values (ϕ was set to 0), are shown in the figure in blue. In green, we show a fit of the simulated data to non-modulated decaying oscillations. The resulting frequency and time-decay are shown in the figure in green.

7 Double pump measurements of SnSe with additional fluences

The main text presents double pump measurements of SnSe at a combination of fluences - 3.55 and 1.20[mJ/cm²] (corresponding to excitation densities of $\approx 6.37 \times 10^{21}$ and 2.15×10^{21} [cm⁻³])⁴⁵ for the leading and trailing pumps respectively. In this section, we show an additional dataset with incident fluences of 4.00 and 0.95[mJ/cm²] (corresponding to excitation densities of $\approx 7.19 \times 10^{21}$ and 1.71×10^{21} [cm⁻³])⁴⁵ for the leading and trailing pump beams respectively. The measurements show qualitatively similar results to those shown in Figure 4 in the main text. The main difference is that the frequencies of the modulations shown in Figure S8 panels (c) and (d) are different than the frequencies presented in Figure 4 panels (c) and (d) in the main text. In all cases they correspond to the frequency of the phonon observed when using only the leading pump.

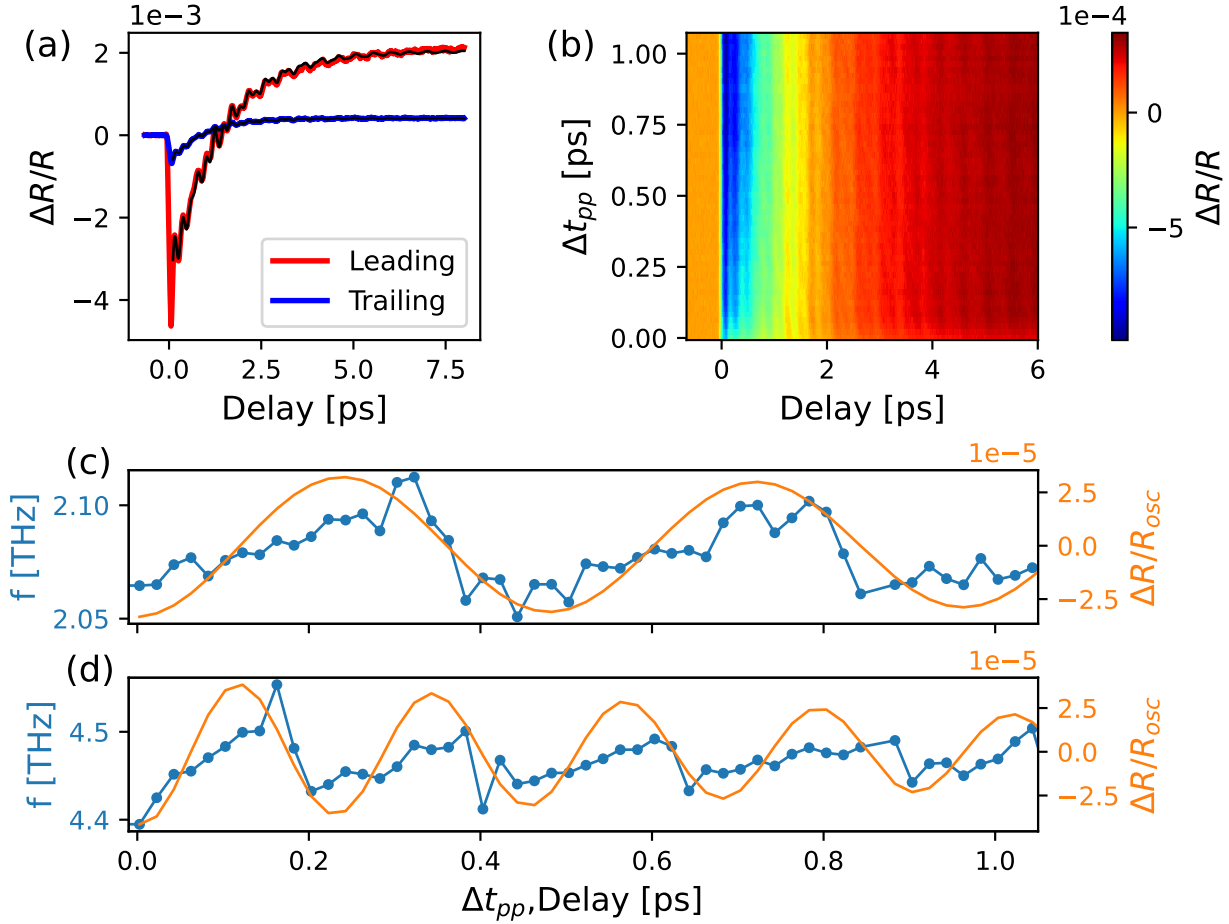


Figure S8: Double pump measurements of SnSe. (a) $\Delta R/R$ data in SnSe, taken with single pump excitation. The blue curve is taken only with the trailing pump whereas the red curve is taken only with the leading pump. (b) Color map of the double pump $\Delta R/R$ data for SnSe. Colors represent the magnitude of $\Delta R/R$, the horizontal axis is the time delay between the probe and the trailing pump whereas the vertical axis is Δt_{pp} . In panels (c) and (d), plots similar to those presented in Figure 3(b) are presented, corresponding to two of the A_g phonons of SnSe. In both panels, the blue curves show the phonons' frequency as a function of Δt_{pp} and the orange curves are the corresponding oscillatory component of $\Delta R/R$ of the leading pump, which were extracted by fitting to the pump-probe data shown in panel (a), as a function of the time delay between the pump and the probe pulses.